Focal Spot Blur Reduction by Deconvolution on CT Projections

Lucas Determan[1], Kirk Busche[1], Pradeep Bhattad[1]

[1]North Star Imaging, Inc., Rogers, MN, United States of America, e-mail: ldeterman@4nsi.com, kbusche@4nsi.com, pbhattad@4nsi.com

Abstract
High-energy X-ray sources typically generate X-rays from a larger focal spot. This enables the imaging of dense objects but can lead to reduced image quality due to increased geometric unsharpness. This paper investigates and compares computational methods for reducing the resulting blur. Two approaches for acquiring the focal spot blur intensity profile are explored, as well as the subsequent removal of the induced blur in the CT projections via deconvolution. The modified CT projections are reconstructed using standard filtered backprojection (FBP) to assess the blur reduction performance. The results of the deconvolution approaches are evaluated both in 2D (projection) space and in 3D (reconstruction) space using spatial resolution, contrast-to-noise, and qualitative analyses.

Keywords: Focal Spot, Deconvolution, Computed Tomography, Blur, Unsharpness

1 Introduction

The increased demand for non-destructive evaluation of high-density parts has necessitated the need for higher energy X-ray systems. However, these industrial high-energy sources generate larger focal spots—up to several millimeters—resulting in more geometric unsharpness. The increase in geometric unsharpness induces blur onto the CT projections resulting in worse spatial resolution. To mitigate this effect, reducing the focal spot size or decreasing magnification could be considered. However, physically reducing the focal spot size is often impractical and decreasing magnification is not always desirable. Therefore, addressing the effects of a large focal spot post-acquisition, such as through computational techniques, becomes an appealing solution.

One such computational technique is solving the inverse problem that arises from formulating the imaging as a convolution process

$$\boldsymbol{y} = \boldsymbol{k} * \boldsymbol{x} + \boldsymbol{n} \tag{1}$$

where $\boldsymbol{k}$ is the focal spot blurring kernel, $\boldsymbol{x}$ is the unknown sharp image, $\boldsymbol{y}$ is the measured blurred image, and $\boldsymbol{n}$ is the observation noise. In optics, this type of inverse problem is well studied, with many approaches using image deconvolution to reduce blur [1]. Deconvolution is a process for recovering the unknown sharp image from the measured blurry image. This operation can be performed with two families of algorithms: non-blind and blind. In the non-blind case, a known theoretical or measured estimate of the point source is used to recover the sharp image. In the blind deconvolution case, both the point source and sharp image are estimated from the measured blurry image. Following the deconvolution procedure, the recovered CT projections are then reconstructed into the CT volume. In this work, both methods for estimating the source blur and subsequent deconvolution of the CT projections with the blur estimate are investigated. These techniques are applied to real-world data acquired from high-energy sources to evaluate the blur reduction performance both quantitatively and qualitatively.

2 Methods

The investigation involved two parts: acquiring the blur model and applying deconvolution. Two different approaches for acquiring the blur model estimate were evaluated, as well as two different deconvolution methods. This paper compares the combination of the four unique methods for the full deconvolution applied to both 2D projections and the reconstructed 3D volume. In the 3D case, the deconvolution was implemented as a preprocessing step to the 2D CT projections before filtered backprojection (FBP).

2.1 Kernel Recovery

Two approaches for acquiring the focal spot model were evaluated: reconstructing using radial rays along the perimeter of a hole [2], [3] [4] and through blind deconvolution using a *maximum a posteriori* (MAP) approach, iteratively estimating the blur model and the unknown image [5].

The radial filtered backprojection (FBP) method reconstructs the focal spot profile from an image of a small circular aperture. A circular aperture provides strong edges in all directions, which are characterized using the local derivatives of rays radially positioned along the circle [3] [4]. The 2D focal spot model can then be constructed by an inverse Radon transform, in this case using FBP. The model, however, needs additional postprocessing to be functional for the subsequent deconvolution

methods as it contains a non-zero background intensity value. Thresholding was applied to the resulting blur image to remove background noise, and cropping was utilized to constrain the spatial impact of the model when deconvolving.

The second method used for reconstructing the focal spot blur model was an iterative blind deconvolution method using a *maximum a posteriori* (MAP) estimation. Let $(\hat{\boldsymbol{x}}, \hat{\boldsymbol{k}})$ be the pair which minimizes the convolution error in (1), which is the solution with maximal a posteriori probability

$$(\hat{\boldsymbol{x}}, \hat{\boldsymbol{k}}) = \arg\max \log p(\boldsymbol{x}, \boldsymbol{k} \,|\boldsymbol{y}). \tag{2}$$

However, as was shown in [1] [5], this formulation often does not provide a satisfactory solution, so they proposed instead to produce a MAP estimate of $\hat{\boldsymbol{k}}$ for kernel sizes sufficiently smaller than the image size

$$\hat{\boldsymbol{k}} = \arg\max p(\boldsymbol{k}|\boldsymbol{y}) = \arg\max p(\boldsymbol{y}|\boldsymbol{k})$$
$$p(\boldsymbol{y}|\boldsymbol{k}) = \int p(\boldsymbol{x}, \boldsymbol{y}|\boldsymbol{k}) d\boldsymbol{x}. \tag{3}$$

Following the work of [5], this paper uses an Expectation-Maximization (EM) model to produce the solution $\hat{\boldsymbol{k}}$ with sparse priors. In theory, this blind deconvolution process would work on any input image, including the CT scan projections. However, in practice these projections may not contain enough edge information, so for better blur model recovery, the circular aperture (hole) image was used with the MAP approach.

2.2 Deconvolution

The estimate of the focal spot $\hat{\boldsymbol{k}}$ was then used in two different deconvolution methods: a direct inverse filtering approach and an iterative approach. In this paper, the regularized Wiener deconvolution [6] was chosen as the direct inverse filtering method. This method leverages the fact that convolution in the spatial domain is equivalent to multiplication in the frequency domain, so (1) becomes

$$\boldsymbol{Y} = \boldsymbol{K}\boldsymbol{X} + \boldsymbol{N}, \tag{4}$$

where the capital letters refer to the Fourier transform of the original signal. The Wiener filter is the filter $\boldsymbol{w}$ which, when convolved with the observed image $\boldsymbol{y}$ gives the estimate $\hat{\boldsymbol{x}}$ which minimizes the mean square error

$$\epsilon = E[\boldsymbol{x} - \hat{\boldsymbol{x}}]^2, \tag{5}$$

and is given in the frequency domain as

$$\boldsymbol{W} = \frac{\boldsymbol{K}^*}{|\boldsymbol{K}|^2 + \lambda}, \tag{6}$$

where $\boldsymbol{K}^*$ denotes the complex conjugate of $\boldsymbol{K}$ and λ is a regularization factor [6]. The deconvolved $\hat{\boldsymbol{x}}$ is then given by

$$\hat{\boldsymbol{x}} = \mathcal{F}^{-1}\{\boldsymbol{W}\boldsymbol{Y}\}. \tag{7}$$

Direct inverse filtering is a fast method of deconvolution, but it is often prone to artifacts such as ringing and relies on a careful choice of the regularization factor λ. To address these shortcomings, constrained iterative deconvolution techniques, such as the Richardson-Lucy method [7], have been developed. In this study, the conjugate gradient approach to solving the E-step of the MAP problem (3) with sparse priors was used for the iterative non-blind deconvolution, with full derivation available in [5].

3 Experiment Setup

The circular aperture image required for the focal spot kernel recovery was acquired by imaging an ASTM plaque-type Image Quality Indicator (IQI). These plaque IQIs are well-suited for this task as they consist of several precisely manufactured holes of varying diameters on a thin plaque. The ray-based reconstruction method for kernel recovery assumes the ideal sharp image is of a perfect circle and attributes any deviation from a perfect edge to the focal spot blur. However, due to the parallax effects inherent in X-ray imaging, this assumption is violated for any real aperture with non-zero depth. Plaque IQIs help minimize this effect due to their thin thickness but are available in a range of materials to ensure sufficient contrast even with such thinness.

Another consideration is alignment of the IQI plate relative to the detector and source to prevent geometric misalignment from contributing to the blur. One straightforward approach to minimizing the geometric misalignment is by following the procedure outlined in ASTM E1165 which acquires the image of plaque IQI under high magnification, aligned parallel to the face of the source [8]. Although acquiring the image of the IQI hole at high magnification will produce a high-quality image of the focal spot, the induced blur by a focal spot on a CT scan is magnification dependent. In (1), $\boldsymbol{x}, \boldsymbol{y},$ and $\boldsymbol{k}$ must all have the same sample size, which in X-ray imaging means the effective pixel pitch must match between all three components. Thus, a high-quality image of the focal spot acquired under high magnification must either be downsampled to match the geometric

magnification of the scan or the corresponding scan radiographs upsampled to the high magnification of the IQI image, but this method is highly sensitive to imperfect geometric magnification calculations. Another complication with simply scaling the blur model $\boldsymbol{k}$ is the compounding sources of blur, namely focal spot blur and detector (scintillator) blur, captured in the estimate of $\boldsymbol{k}$. Although scaling $\boldsymbol{k}$ to the appropriate geometric magnification would properly scale the focal spot blur, the detector blur would be improperly scaled as the detector blur is magnification independent. For these reasons, this paper chose an alternative route to capturing the plaque IQI image—acquiring the image at the same geometric magnification as the CT scan, with careful positioning to ensure sufficient geometric alignment to reduce parallax.

Two different systems were used in this investigation, with a unique object scanned on each due to differing X-ray penetration powers. The first object was an additively manufactured (AM) titanium lattice scanned using an NSI X5000 with a 450 kV MesoFocus X-ray source, with a nickel plaque IQI used to image the blur model, shown on the left in Figure 1: Left is the AM lattice cylinder scanned with the NSI X5000 450 kV source and on the right is the RQI cylinder imaged on the high energy 9 MeV source. Figure 1. The second object was an AM Representative Quality Indicator (RQI) consisting of a cylinder with several spherical voids of varying diameters embedded made from tungsten, shown on the right in Figure 1. This RQI was scanned using an NSI MeVX system with a 9 MeV linear accelerator (LINAC) as the X-ray source, using a tungsten plaque IQI for the circular aperture acquisition. Table 1 contains the scan parameters used for both CT scans, as well as information pertaining to the plaque IQI material and aperture size. Data collection was done by acquiring the plaque IQI image for blur model recovery immediately adjacent to the CT scan, in order to minimize any variations in the system.

Table 1: Systems and scan parameters used.

		AM Lattice Cylinder	AM Cylinder RQI
NSI System		X5000	MeVX9
Part	Material	Titanium	Inconel
Hole	Material	Nickel	Tungsten
	Dimensions	3.048 mm	6.223 mm
Source	Model	Comet iVario MesoFocus 450 kV	Linatron M9 9 MeV
	Voltage	200 kV	9 MeV
	Current/PPS	2000 µA	344 PPS
Detector	Model	Varex XRD 4343N	Varex Industrial 4343HE
	Pixel Size	150 µm	139 µm
	FPS	14.61	0.88
	Frame Avg.	25	10
Scan	Magnification	3.12x	2x
	Projections	2300	720

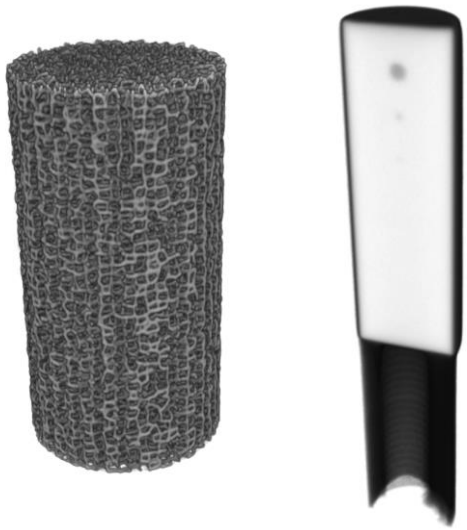

Figure 1: Left is the AM lattice cylinder scanned with the NSI X5000 450 kV source and on the right is the RQI cylinder imaged on the high energy 9 MeV source.

Both methods for recovering the blur model were applied to each plaque IQI image. Using the recovered blur models, both deconvolution methods were applied to each scan's radiographs prior to the FBP reconstruction. The reconstructed volumes were evaluated based on the qualitative slice data. Due to the cylindrical nature of the tungsten RQI, ASTM E1695 [9] was used

for quantitative analysis of deconvolution methods impact on spatial resolution and contrast to noise ratio (CNR). In addition to 3D data, line pair gauge images were captured on the high-energy 9 MeV system using the same scan parameters as the CT scan, enabling a quantitative 2D measurement.

4 Results

The first object considered is the titanium AM lattice cylinder scanned using the 450 kV MesoFocus source. The lattice structure contains numerous edge features which are useful for comparing the deconvolution results. Figure 2 shows the IQI hole image used to obtain the blur model for this scan, with its respective pixel intensity histogram. To establish sufficient contrast while maintaining the desired scan parameters of the CT scan, a nickel plaque IQI was chosen.

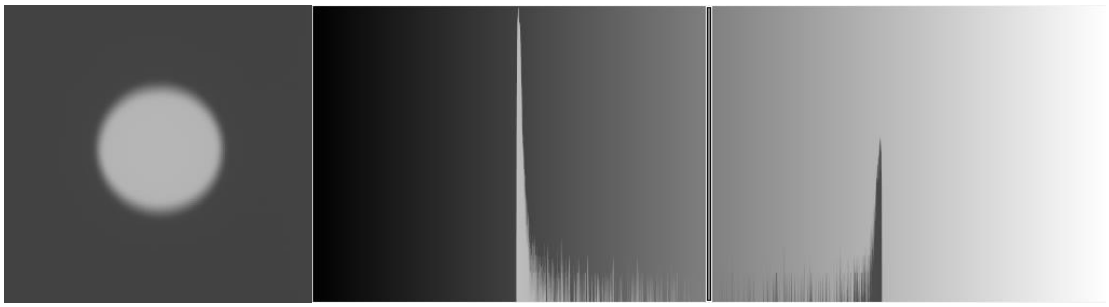

Figure 2: Original image from 450 kV IQI plate hole for AM Lattice part with the intensity histogram.

The blur models were estimated following the two methods described in Section 2.1: radial filtered backprojection (FBP) and iterative blind deconvolution (IBD). The results of both recovery methods are shown in the first row of Figure 3 and show some significant differences in both the shape and intensity, particularly in the exterior “wings” of the IBD model. Over the initial iterations of the IBD method, the blur estimates were similar to the FBP estimate, but then diverged as the algorithm completed. Figure 3 shows the Wiener deconvolution applied to the IQI image using each of the blur models in the second row, and the IQI image deconvolved with the blur models using conjugate gradient deconvolution (CGD). Visually, it appears the radial FBP technique coupled with the Wiener deconvolution reduces the most blur. However, this combination also produces ringing artifacts which inddicates that the measured model still has signficant deviations from the true blur model. The other deconvolved images also show different artifacts where the right column has a strong ring artifact immediately on the edge of the hole. The radial FBP kernel with CGD appears to reduce the artifacts and noise amplification, but reducing the sharpening of the image relative to the radial FBP kernel and Wiener deconvolution. Due to the poor performance of the IBD kernel recovery on the 2D IQI image, the 3D reconstructions were only performed using the blur model recovered from radial FBP with both Wiener deconvolution and CGD.

(a)

(b)

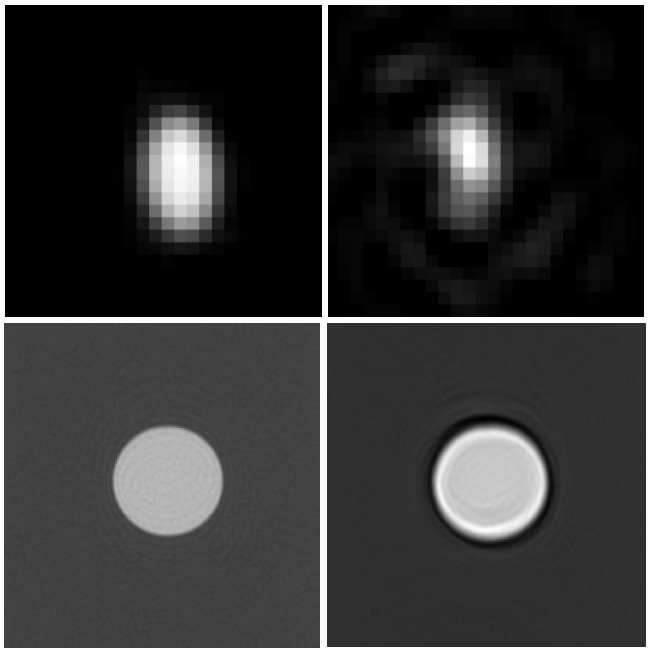

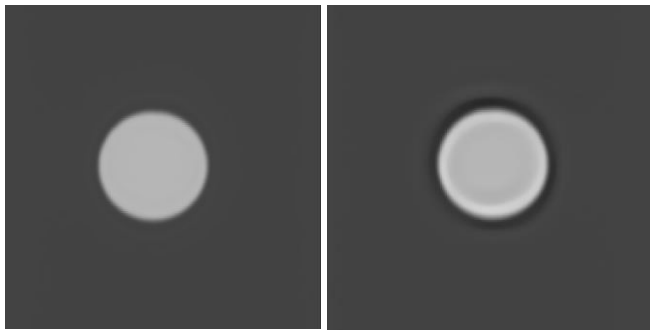

(c)

Figure 3: Left column: blur model using radial FBP and right column the blur model is obtained from IBD, with (a) the obtained blur models, (b) the IQI image deconvolved with Wiener filter and the respective blur models, and (c) the IQI image deconvolved with CGD and the respective blur models.

To evaluate the deconvolution performance, a baseline reconstruction using the original unmodified radiographs was performed for comparison. The slices shown in Figure 4 show slices of the volume within the lattice structure with the different deconvolution techniques using the blur model recovered from the radial FBP method. The performance of the methods is significantly different, with the Wiener deconvolution technique significantly reducing the blur, which is unsurprising given the comparable results in 2D on the IQI hole. Features that are difficult to make out in the baseline are now more apparent in the Wiener filtered deconvolution volume. However, the deconvolution process also introduced artifacts in the air between the lattice structures and amplified the noise present. The artifacts appearing with the Wiener deconvolution are likely attributed to the ringing artifacts present in the 2D images, due to the imperfect estimate of the blur model. This technique does not regularize the noise beyond the configurable scalar λ, resulting in its amplification at certain frequencies. The CGD method does not reduce the blur as dramatically as the Wiener deconvolution but does appear to partially reduce it. This method also introduces additional artifacts, visible in the air gaps between the lattice structure.

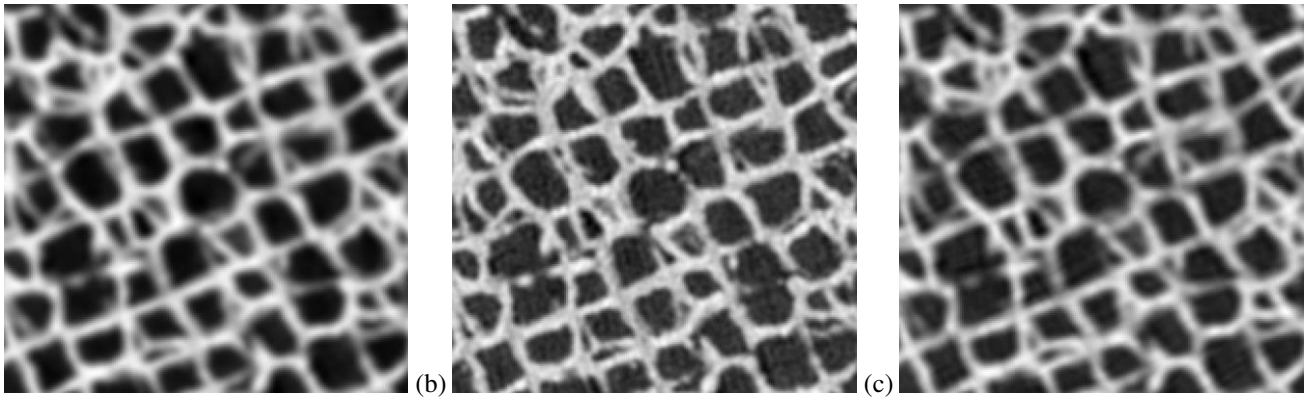

(a) (b) (c)

Figure 4: AM Lattice Cylinder Y Slice of CT reconstruction (a) baseline no deconvolution, (b) Wiener deconvolution, and (c) conjugate gradient deconvolution.

Another slice from this scan is shown in Figure 5 which shows the 3D printed plastic fixture used to hold the AM lattice. It is apparent that once again Wiener deconvolution produces the most improvement in reducing the blur while the CGD has a less pronounced effect. The artifacts from the Wiener deconvolution, however, are considerably more prominent with each high contrast feature producing some ringing artifacts. Additionally, the background intensity and noise are also greatly impacted. The CGD slice again shows less significant blur reduction but with fewer artifacts and noise enhancement when compared to the Wiener deconvolution results. These slices paired with the IQI hole images suggest that sufficient blur reduction can be achieved using the FBP kernel recovery and Wiener deconvolution. However, the noise amplification and the introduction of new artifacts due to the imperfect blur model combined with the Wiener deconvolution may surpass any improvements in sharpness for certain applications. Similarly, the FBP kernel recovery with the CGD approach did not show significant blur reduction, while requiring additional imaging (plaque IQI image acquisition) and processing time. Parameters for the deconvolution were selected based on the 2D data, additional parameter adjustments could be made to further improve the 3D results.

(a) 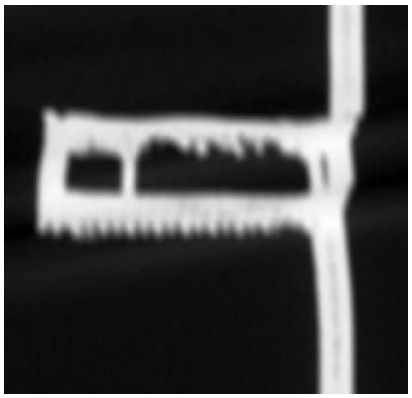 (b) 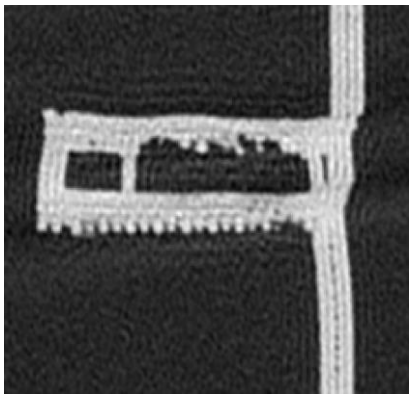 (c) 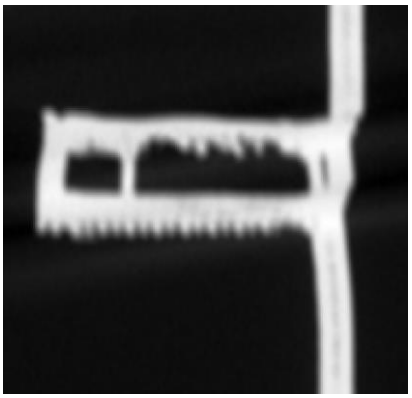

Figure 5: AM lattice cylinder X slice of CT reconstruction (a) baseline no deconvolution, (b) Wiener filter, and (c) conjugate gradient deconvolution.

An NSI MeVX high-energy system with a 9 MeV source was also used to collect images for both 2D and 3D analysis. The circular aperture image required for the blur model recovery was acquired by imaging a hole in a sheet of tungsten plating for sufficient contrast. The blur models were once again reconstructed from the hole image using both methods and are shown in Figure 6. An additional spatial resolution image consisting of a line pair gauge was acquired at the same geometric magnification as the CT scan and hole image. Again, the four combinations of blur model recovery and deconvolution techniques were used, with Figure 7 depicting the visual results on the line pair gauge and showing the impact on the noise and ringing. It is apparent that the CGD techniques reduce the amplified noise relative to the Wiener deconvolution results. The spatial resolution results, calculated following the procedure of ASTM E2002 [10], are shown in Figure 8 and demonstrate the Wiener deconvolution significantly improved the numerical spatial resolution results. This is also visually confirmed in the 2D radiographs of the line pair gauge in Figure 7. From the spatial resolution results and the depiction of the blur models in Figure 6, the choice of deconvolution technique dominated the impact on spatial resolution relative to the choice of blur model.

(a) 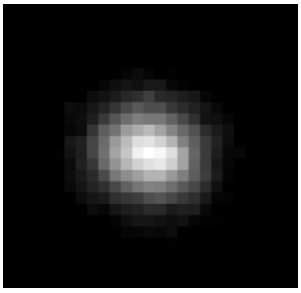 (b) 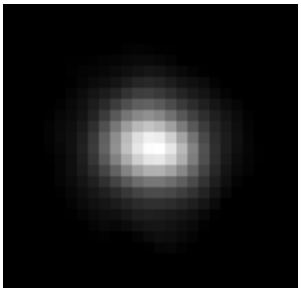

Figure 6: Blur models for high-energy 9 MeV source (a) radial FBP and (b) IBD.

(a) 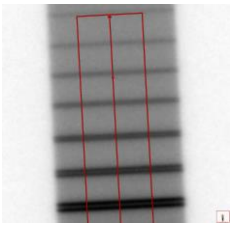 (b) 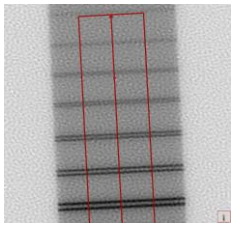 (c) 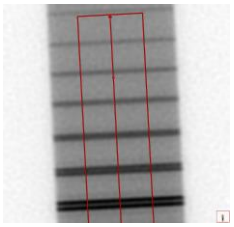 (d) 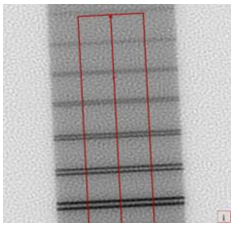 (e) 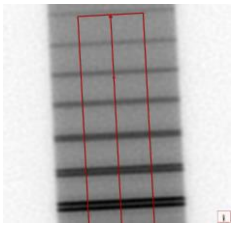

Figure 7: Spatial resolution line pair gauge DR image for: (a) baseline, (b) radial backprojection with Wiener filter, (c) radial backprojection with CGD, (d) IBD with Wiener filter, and (e) IBD with CGD.

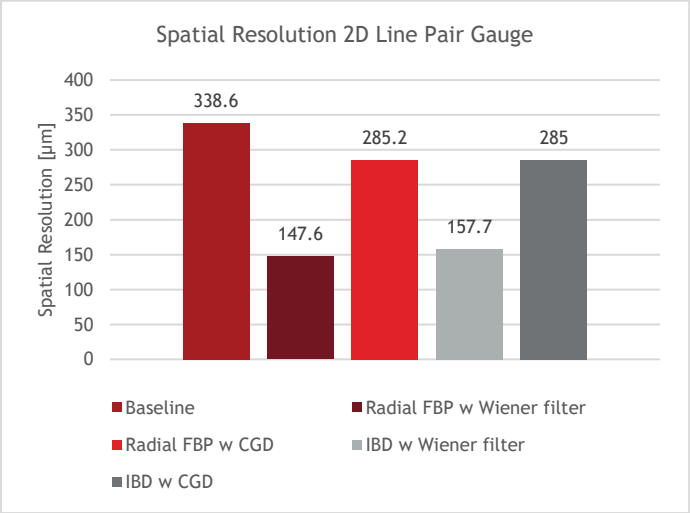

Figure 8: Spatial resolution results measured from the 2D radiographs with a line pair gauge.

Reconstructions of the RQI cylinder were performed for each combination of model and deblur. The RQI cylinder contains spherical voids and sections of homogenous material, enabling evaluation of the deconvolution combinations from both a feature-resolution approach and a numerical spatial resolution approach using ASTM E1695. Figure 9 shows a slice from each reconstruction of the RQI cylinder containing one of the spherical voids. From these slices, it is visible that both Wiener deconvolution methods greatly enhance both the edge responses and the noise response, whereas the CGD methods suppress the noise response better while providing significant edge enhancement. In addition to visually assessing the techniques, ASTM E1695 was performed on a slice from each reconstruction without a spherical void present. The spatial resolution and CNR results from these analyses are shown in Figure 10 and indicate that the choice of deconvolution method dominates the numerical results relative to the choice in method for obtaining the blur, with the CGD method outperforming the Wiener deconvolution on both metrics regardless of kernel choice. However, these ASTM E1695 results can be misleading, as the procedure does not robustly determine the true spatial resolution when artifacts such as ringing are present. For the CGD slices shown, the reconstructions have significant ringing artifacts concentrated on the outer edge of the cylinder, which artificially enhances the edge response function due to the overshooting. This makes it difficult to fairly assess the spatial resolution of the different methods in 3D using ASTM E1695, making these results inconclusive.

(a) 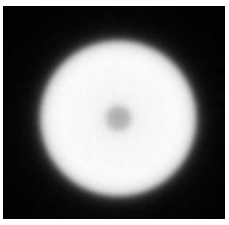 (b) 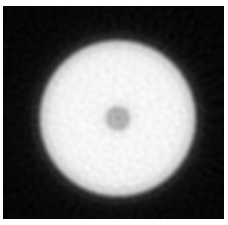 (c) 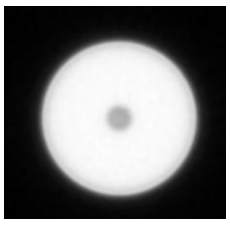 (d) 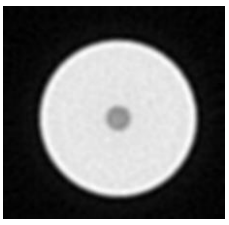 (e) 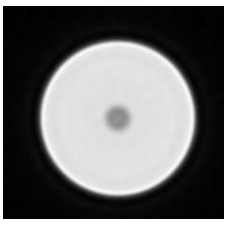

Figure 9: AM RQI cylinder slice of CT reconstructions (a) baseline no deconvolution, (b) FBP model with Wiener deconvolution, (c) FBP model with CGD, (d) IBD model with Wiener deconvolution, and (e) IBD model with CGD.

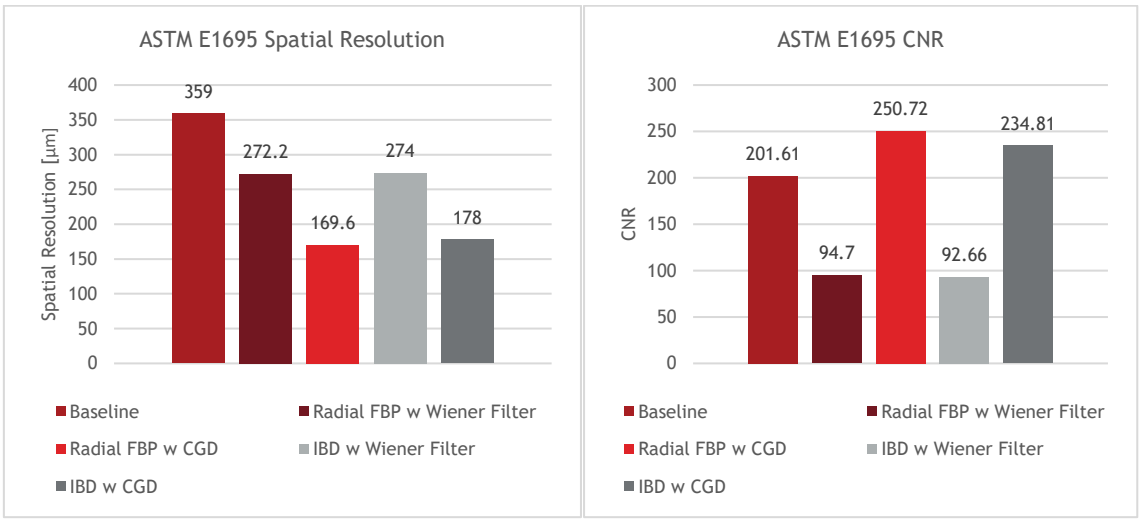

Figure 10: ASTM E1695 analysis of spatial resolution and CNR on RQI cylinder.

Figure 11 shows a slice through the volume with a line profile across the cylinder fixturing, to enable evaluation on four edges, with the corresponding line profile results from the baseline reconstruction and the reconstructions from each deconvolution combination. The Wiener deconvolution results show the noise in the slice is once again amplified while enhancing the edges. Again, the CGD results show better noise suppression relative to both the baseline reconstruction and the Wiener deconvolution results, while not achieving as impressive edge enhancement. The focal spot model obtained from IBD does appear to introduce ringing in both deconvolution techniques which suggests the estimated blur model is not a sufficient representation of the actual blur.

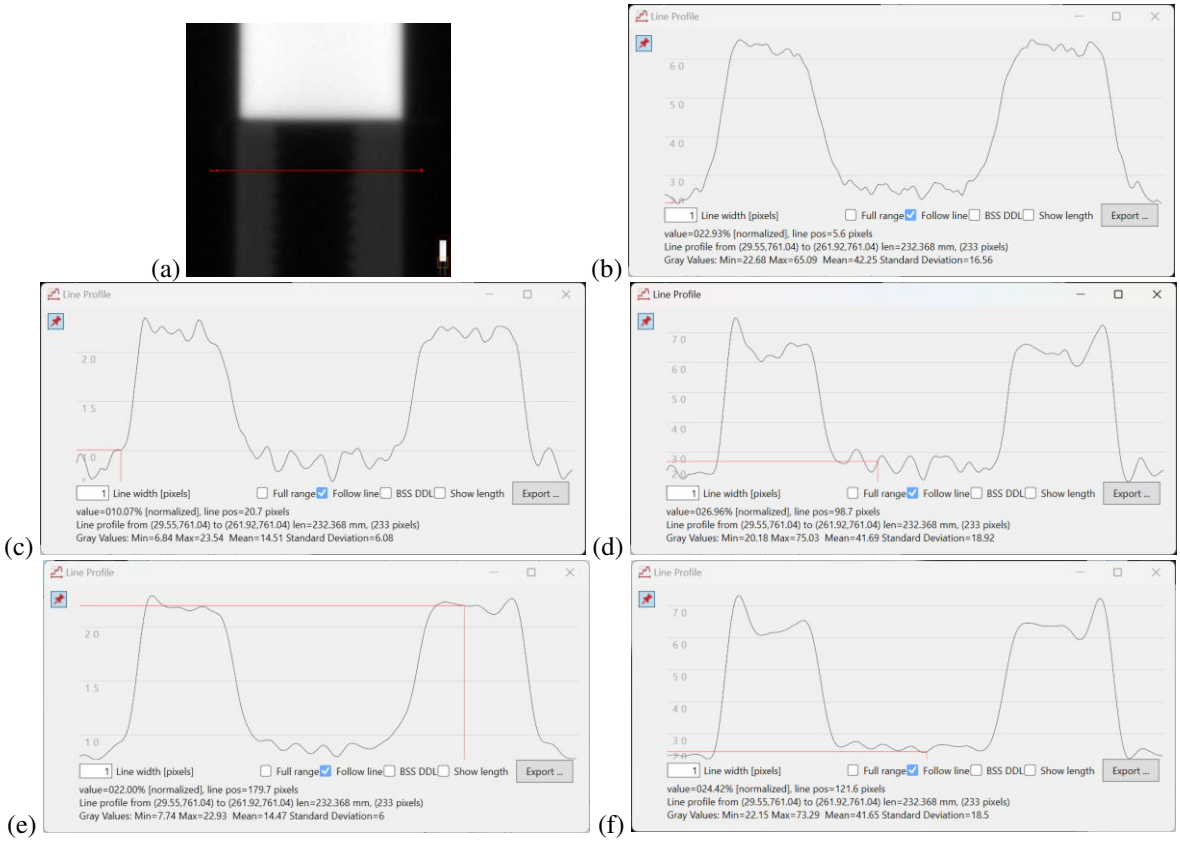

Figure 11: RQI slice with line profile across the walled fixturing with (a) the slice from the baseline reconstruction, and the line profile plots for (b) the baseline reconstruction, (c) radial FBP model with Wiener deconvolution, (d) IBD model with Wiener deconvolution, (e) radial FBP model with CGD, and (f) IBD model with CGD.

5 Conclusion

Obtaining an accurate model of an X-ray system's focal spot which can be properly applied to the acquired projections is not trivial. Slight changes to the shape, size, or intensity of the blur model significantly impact the performance of the deconvolution procedure, introducing significant artifacts such as ringing. The methods for recovering the blur model are highly dependent on proper alignment to minimize parallax blur and the identification of the plaque IQI hole edges in the image. Since deconvolution is an ill-posed problem, this procedure is highly sensitive to small perturbations like noise, both in the blur model and the projection data. Direct inverse filtering paired with the radial ray reconstruction of the focal spot using a technique like [2] [3] is therefore insufficient for real-world applications without additional processing. The real-world data suggests additional processing and/or techniques should be used to obtain a more accurate definition of the blur model as well as to reduce the noise on the X-ray data.

Overall, the results from this work show that applying the blur model improved the spatial resolution of the resulting projections. The ability to do this with minimal artifacts depends on the techniques used throughout the procedure, including in recovering the focal spot model and in methods for applying the model. Noise was a significant factor in recovering a CT projection effectively and the techniques studied show the impact of the noise can outweigh the improvements in the spatial resolution for many applications. Future works will focus on approaches to mitigate the impact of noise on the deconvolution procedure, such as denoising, and alternatives to deconvolution to utilize the focal spot image for deblurring.

References

[1] A. Levin, Y. Weiss, F. Durand and W. T. Freeman, "Understand and evaluating blind deconvolution algorithms," *IEEE Conference on Computer Vision and Pattern Recognition,* pp. 1964-1971, 2009.

[2] T. S. Cho, S. Paris, B. K. P. Horn and W. T. Freeman, "Blur Kernel Estimation using the Radon Transform," *CVPR,* pp. 241-248, 2011.

[3] B. A. Bircher, F. Meli, A. Kung and A. Sofiienko, "Traceable x-ray focal spot reconstruction by circular edge analysis: from sub-microfocus to mesofocus," *Measurement Science and Technology,* vol. 33, no. 074005, 2022.

[4] G. Di Domenico, P. Cardarelli, A. Contillo, A. Taibi and M. Gambaccini, "X-ray focal spot reconstruction by circular penumbra analysis—Application to digital radiography systems," *Medical physics,* vol. 43, p. 294–302, 2016.

[5] A. Levin, Y. Weiss, F. Durand and W. T. Freeman, "Efficient Marginal Likelihood Optimization in Blind Deconvolution," *CVPR 2011,* pp. 2657-2664, 2011.

[6] N. Wiener, Extrapolation, interpolation, and smoothing of stationary time series: with engineering applications, The MIT press, 1949.

[7] W. H. Richardson, "Bayesian-based iterative method of image restoration," *JoSA,* vol. 62, p. 55–59, 1972.

[8] *ASTM E1165 - 12 (Reapproved 2017), Standard Test Method for Measurement of Focal Spots of Industrial X-Ray Tubes by Pinhole Imaging,* West Conshohocken, PA: ASTM International, 2017.

[9] *ASTM E1695 - 20e1, Standard Test Method for Measurement of Computed Tomography (CT) System Performance,* West Conshohocken: ASTM International, 2020.

[10] *ASTM E2002 - 15, Standard Practice for Determining Total Image Unsharpness and Basic Spatial Resolution in Radiography and Radioscopy,* West Conshohocken: ASTM International, 2015.